

Fast and Explicit Neural View Synthesis

Pengsheng Guo
Apple
pengsheng_guo@apple.com

Miguel Angel Bautista
Apple
mbautistamartin@apple.com

Alex Colburn
Apple
alexcolburn@apple.com

Liang Yang
Apple
ericyang@apple.com

Daniel Ulbricht
Apple
dulbricht@apple.com

Joshua M. Susskind
Apple
jsusskind@apple.com

Qi Shan
Apple
qshan@apple.com

Abstract

We study the problem of novel view synthesis of a scene comprised of 3D objects. We propose a simple yet effective approach that is neither continuous nor implicit, challenging recent trends on view synthesis. We demonstrate that although continuous radiance field representations have gained a lot of attention due to their expressive power, our simple approach obtains comparable or even better novel view reconstruction quality comparing with state-of-the-art baselines while increasing rendering speed by over 400x. Our model is trained in a category-agnostic manner and does not require scene-specific optimization. Therefore, it is able to generalize novel view synthesis to object categories not seen during training. In addition, we show that with our simple formulation, we can use view synthesis as a self-supervision signal for efficient learning of 3D geometry without explicit 3D supervision.

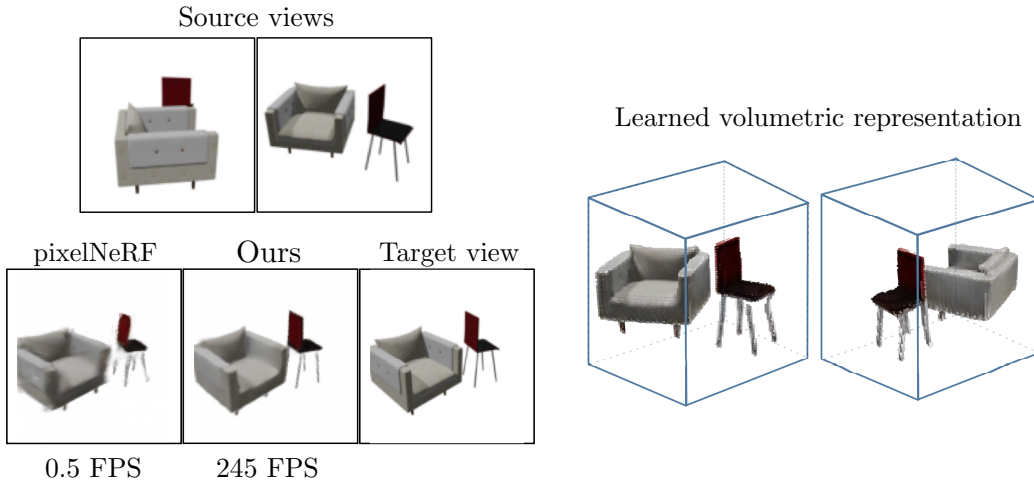


Figure 1: Our model performs scene-agnostic and category-agnostic novel view synthesis in real time. A complete 3D geometry of the scene is estimated through a single forward pass. Our model consistently produces higher quality results comparing to the state-of-the-art view synthesis approach pixelNeRF [1], while being over 400x faster in rendering time.

1 Introduction

In order to understand the 3D world, an intelligent agent must be able to perform inference about a scene’s appearance and shape from unseen viewpoints. Being able to synthesize images at target camera viewpoints efficiently given sparse source views serves a fundamental purpose in building intelligent visual behaviour [2, 3, 4]. The problem of learning to synthesize novel views has been widely studied in literature, with approaches ranging from traditional small-baseline view synthesis relying on multi-plane imaging [5, 6, 7, 8], flow estimation [9, 10], to explicitly modeling 3D geometry via point-clouds [11], meshes [12], and voxels [13].

A recent wave of approaches for view synthesis have adopted continuous radiance field representations [1, 14, 15, 16, 17], where scenes are represented as a continuous function that shares its domain with the signal being fitted (e.g. a function that takes points in \mathbb{R}^3 as input, to model a 3D signal), as opposed to discrete representations where the 3D signals are encoded in a discrete geometric structure like a volume [13] or a mesh [12]. Although continuous radiance field representations enjoy the benefits of being resolution-free or modeling view-dependent effects, they are not efficient for real-world use cases that require real-time performance. Typically, radiance field representations suffer from one of the following two issues. First, being computationally costly to obtain when implicitly modeled [15, 17, 18], e.g. the model parameters are optimized via gradient descent for each object or scene, usually taking tens of hours on commodity hardware. Second, not being able to amortize the rendering cost across views, since radiance fields are evaluated independently for every pixel being rendered [1, 16]. This dramatically impacts the practicality of radiance field, since rendering an image can take seconds on modern GPUs.

A natural question arises: *Are there viable alternatives to continuous radiance fields with unique advantages?* To answer this question, we introduce a simple yet effective approach to perform novel view synthesis that is neither continuous nor implicit. Our approach enjoys the following benefits: (i) the scene representation is fast to obtain, as it does not require gradient-based optimization for new scenes, and (ii) it is efficient to render, since it models the complete 3D geometry and appearance in a single forward pass, allowing for amortized rendering. Our experiments show that despite the simplicity of our method, our performance notably matches or beats recent state-of-the-art baselines based on continuous scene representations across different metrics and settings, producing accurate novel view reconstruction, while rendering objects over 400x faster than its closest performing counterpart, pixelNeRF [1]. In addition, we find that the 3D geometry learned by our model in an unsupervised manner (i.e. without the need to train with 3D geometry supervision) is extremely compelling and very practical to obtain, requiring only a single forward pass of the model.

2 Related Work

Learning to synthesize novel views of an object or a scene given one or more sparse observation has been widely studied in the literature [5, 6, 7, 8, 19, 9, 20, 10, 13, 21, 11, 14]. A unifying problem definition for this set of approaches is to predict a target view given a source view/s, conditioned on a relative camera transformation. One set of approaches focuses on small and/or wide baseline view synthesis where the goal is to synthesize a parallax effect by using multi-plane imaging [5, 6, 7], local light-field fusion [8] or cost volume estimation [19]. Another set of approaches focuses on learning a free-form 2D flow field that takes pixels from a single [9] or multiple source views [10] and reconstructs a target view given the relative camera transformation between source/s and target. A modification of such approaches was concurrently proposed in [13] and [21], where instead of predicting a 2D flow-field, these methods predict a latent 3D representation (in the form of a feature volume) to which the relative camera transformation from source to target view can be readily applied. Approaches that model a latent 3D representation enjoy the benefit of being able to model 3D geometry without the need of explicit supervision [22].

In a separate category, implicit representations that model continuous radiance fields for view interpolation [15, 17, 18, 23] have been proposed. These approaches learn a radiance field for every scene or object by fitting the parameters of a model (using gradient descent) to a dense set of views of a scene and then interpolating between those views. Note that this setting is different from the novel view synthesis setting where the problem is to predict a target view given a source view and a relative camera transformation. However, recent approaches have applied continuous radiance fields

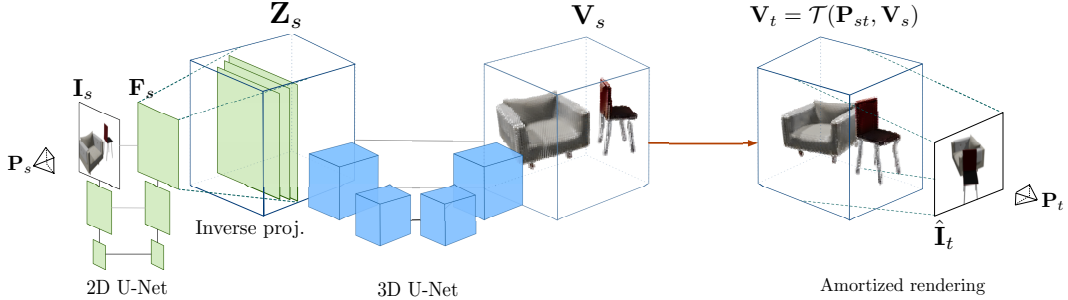


Figure 2: Our model is comprised of three main components: a) a 2D U-Net image encoder, b) a 3D U-Net scene encoder, and c) an amortized rendering process. The 2D U-Net encoder generates a 2D feature map \mathbf{F}_s from the input image \mathbf{I}_s . The feature map is then projected into a latent volume \mathbf{Z}_s via an inverse project step. A 3D U-Net network maps \mathbf{Z}_s into an $\text{RGB}\alpha$ volume \mathbf{V}_s . This $\text{RGB}\alpha$ volume is applied a relative pose transformation \mathbf{P}_{st} to match the target view pose \mathbf{P}_t , and the resulting image $\hat{\mathbf{I}}_t$ is created by rendering the $\text{RGB}\alpha$ using a simple volume rendering process that is amortized across views.

to the novel view synthesis problem [1, 15, 16], showing that it is possible to model multiple objects or scenes within a single model and extrapolating to object categories unseen during training.

We can group recent approaches to novel view synthesis with implicit and continuous radiance field representations into two mutually exclusive categories. In the first category we find approaches that provide an efficient approach to explicitly encode source views into a continuous representation but are inefficient during rendering due not being able to amortize the rendering process across views [1, 16, 24] (see Sect. 3.3 for details). In the second category, we find recent approaches that enable efficient rendering [25, 26, 27] but where their continuous representation is implicit, and must be fitted via gradient descent for every new object or scene (typically taking days on commodity hardware). In this paper we present a simple yet powerful approach for novel view synthesis which explicitly encodes sources views into a volumetric representation that enables amortized rendering. Thus combining the best of both types of recent approaches for novel view synthesis.

3 Methodology

The novel view synthesis problem is defined as follows. Given a set $\mathcal{S} = \{(\mathbf{I}_i, \mathbf{P}_i)\}_{i=0}^n$ of one or more source views, where a view is defined as an image $\mathbf{I}_i \in \mathbb{R}^{3 \times h \times w}$ together with its pose $\mathbf{P}_i \in \text{SO}(3)$, we want to learn a model f_θ that can reconstruct a ground-truth target image \mathbf{I}_t conditioned on its pose \mathbf{P}_t , where the predicted target image is obtained as $\hat{\mathbf{I}}_t = f_\theta(\mathcal{S}, \mathbf{P}_t)$.

We design f_θ as a simple fully convolutional model that allows amortized rendering. Our model processes a source view through a 2D U-Net encoder [28] to produce a feature map that is projected onto a latent volumetric representation via an inverse projection step. This volumetric representation is further processed with a 3D U-Net model to learn an $\text{RGB}\alpha$ volume¹ to which the relative pose transformation between source and target views is applied, and finally rendered into the predicted target view. We illustrate our pipeline in Fig. 2.

3.1 Encoding

The initial step of our model is to encode the source $\mathbf{I}_s \in \mathbb{R}^{3 \times h \times w}$ with a fully convolutional U-Net encoder that produces a feature map $\mathbf{F}_s \in \mathbb{R}^{c \times h \times w}$ that preserves the spatial resolution of the source image. Once a feature map \mathbf{F}_s is obtained, we perform an inverse projection step to back-project \mathbf{F}_s into a latent volumetric tensor $\mathbf{Z}_s \in \mathbb{R}^{c \times d_s \times h_s \times w_s}$, where d_s, h_s, w_s are depth, height and width for the volumetric representation². Instead of reshaping 2D feature maps into a 3D volumetric representation like ENR [13], we found that using an inverse projection step is beneficial to preserve the 3D geometry and texture information (Cf. 4 for empirical evidence).

¹Note that we do not supervise training with an $\text{RGB}\alpha$ volume, the model is forced to learn the $\text{RGB}\alpha$ volume through the rendering process.

²We used intrinsic camera parameters for the inverse projection step, which we assume to be constant.

3.2 Learning a Renderable Volume

After the inverse projection step we simply process \mathbf{Z}_s with a 3D U-Net [29] model and predict a final volume $\mathbf{V}_s \in \mathbb{R}^{4 \times d_s \times h \times w}$. At this stage \mathbf{V}_s encodes an RGB α volume of the object or scene that can be efficiently rendered. Similar to [1, 13] we apply the relative transformation $\mathbf{P}_{st} = \mathbf{P}_t \mathbf{P}_s^{-1}$ between source and target camera poses to the volumetric representation \mathbf{V}_s to obtain a transformed volumetric representation \mathbf{V}_t that is aligned with the target view. We define this transformation operation as a function $\mathcal{T}(\mathbf{P}, \mathbf{V})$ that takes as input a rigid transformation $\mathbf{P} \in SO(3)$ and a volume \mathbf{V} and applies the rigid transformation to the volume. Note that we define $\mathbf{P} \in SO(3)$, however, our formulation naturally extends to other transformations groups (e.g. non-rigid or free-form deformations).

3.3 Amortized Rendering

We now turn to the task of rendering an RGB α volume \mathbf{V} into an image. Recent work on modeling scenes with continuous neural radiance fields [15] has shown great results by using the rendering equation [30] in order to model pixels. At rendering time, [15] propose to obtain a pixel value by tracing the camera ray \mathbf{r} from the near plane t_n to the far plane t_f , and the expected color of a 2D pixel can be calculated as follows (see [15] for details):

$$C(\mathbf{r}) = \int_{t_n}^{t_f} T(t) \sigma(\mathbf{r}(t)) \mathbf{c}(\mathbf{r}(t), \mathbf{d}) dt, \text{ where } T(t) = \exp\left(-\int_{t_n}^t \sigma(\mathbf{r}(s)) ds\right), \quad (1)$$

where $T(t)$ denotes the accumulated transmittance between the near plane and the current point $\mathbf{r}(t)$ along the ray. In practice, numerical quadrature and stratified sampling strategies are adopted to discretize the continuous integral and make the computation viable.

However, a critical problem of the sampling process in NeRF [15] is that it prevents the rendering process to be *amortized* across views. This is because each ray integral in Eq. 1 is independent and points sampled to approximate one ray integral are not reusable for other ray integrals in the scene. Our approach side-steps the need to perform sampling by modelling the scenes complete geometry and appearance as an RGB α volume $\mathbf{V} \in \mathbb{R}^{4 \times d_s \times h \times w}$. This allows us to amortize rendering across views (since all rendered images of a scene share the same RGB α volume) obtaining dramatic rendering speed improvements without sacrificing reconstruction accuracy with respect to recent baselines [1].

Before rendering our RGB α volume \mathbf{V} , we apply a perspective deformation (using intrinsic camera parameters) on the viewing frustum using inverse warping and trilinear sampling [31] (see Appendix for details). For a given pixel location (i, j) , the expected color \hat{C} is calculated as:

$$\hat{C}_{i,j} = \sum_{k=1}^{d_s} T_{i,j}^k \alpha_{i,j}^k \mathbf{c}_{i,j}^k, \text{ where } T_{i,j}^k = \prod_{m=1}^{k-1} (1 - \alpha_{i,j}^m), \quad (2)$$

where $\mathbf{c}_{i,j}^k$ is the color value encoded in the first 3 channels of \mathbf{V}_t and $\alpha_{i,j}^k$ is the value at the last channel.

3.4 Multiple View Aggregation

Our model can take an arbitrary number of source views in \mathcal{S} as input. In order to do so, we first obtain latent volumes \mathbf{Z}_i for each source view. We then take an arbitrary source view s^* in the set of source views as the origin of the coordinate system. Latent volumes \mathbf{Z}_i are then aligned to the origin using the relative transformation \mathbf{P}_{is^*} between corresponding source pose \mathbf{P}_i and origin pose \mathbf{P}_{s^*} . We then pool the aligned volumes by taking the mean across views:

$$\bar{\mathbf{Z}} = \frac{1}{n} \sum_{i \in \mathcal{S}} \mathcal{T}(\mathbf{P}_{is^*}, \mathbf{Z}_i) \quad (3)$$

Finally, the pooled volumetric latent $\bar{\mathbf{Z}}$ is fed to our 3D U-Net to generate an RGB α volume \mathbf{V} which can be efficiently rendered as outlined in Sect. 3.3.

3.5 Training

Similar to [13, 1], we sample tuples of source and target views together with their relative transformation $(\mathbf{I}_s, \mathbf{I}_t, \mathbf{P}_{st})$ during training. We use the model f_θ to predict the target from source $\hat{\mathbf{I}}_t = f_\theta(\mathbf{I}_s, \mathbf{P}_{st})$ and minimize a rendering loss. The rendering loss is a weighted sum of ℓ_2 loss and SSIM [32] loss, defined as

$$\mathcal{L}_{\text{render}} = \sum_t \|f_\theta(\mathbf{I}_s, \mathbf{P}_{st}) - \mathbf{I}_t\|_2^2 + \lambda \mathcal{L}_{\text{ssim}}(f_\theta(\mathbf{I}_s, \mathbf{P}_{st}), \mathbf{I}_t) \quad (4)$$

One advantage of our formulation is that it supports the use of structural losses like SSIM [32] during training. The SSIM loss has been previously proved useful for view synthesis [13], and are not directly applicable to NeRF-like methods [1], as they randomly sample sparse rays from each image during training due to the computational constraints.

4 Experiments

Our model is evaluated on a series of well established ShapeNet³ [33] benchmarks where it achieves similar or better visual quality compared to the state-of-the-art method pixelNeRF [1] and other recent baselines [13, 14], while rendering objects in real time. We also evaluate the 3D reconstruction capabilities of our model, where it outperforms baseline unsupervised 3D reconstruction models. The following sections detail evaluations on category-specific view synthesis for scenes with single and multiple objects, as well as category-agnostic, multi-category, and unseen-category objects. 3D reconstruction is evaluated in Section 4.2, and the design and effectiveness of different components of our model are discussed in Section 4.3.

4.1 Novel View Synthesis

In the novel view synthesis experiments we compare our approach with several state-of-the-art techniques: ENR[13], pixelNeRF [1], DVR [34], and SRN [14]. Our SSIM, PSNR, and LPIPS [35] scores demonstrates that we produce comparable or better rendering quality than pixelNeRF [1] with an explicit volumetric scene representation, while increasing the rendering speed $100\times$ per view, allowing us to render scenes in real-time as show in Table 3.

4.1.1 Category-Specific View Synthesis of Single Objects

We evaluate our model on the ShapeNet chairs and cars categories in single-view and two-view settings, following the same experimental protocol as baseline methods [14, 13, 1]. These category-specific datasets contain 6, 591 different chairs and 3, 514 different cars. Each object has 50 views sampled uniformly on the full sphere, rendering images resolution 128×128 pixels.

Following pixelNeRF, we train a single model for both the single-view and two-view settings. During training, we randomly choose either one or two source views to predict the target view. For evaluation, we use either one or two source views of an unseen object and predict 250 target views. Additionally, we also report the rendering time comparison between pixelNeRF and our method.

Despite its simplicity, our model obtains very competitive results compared to pixelNeRF, as shown in Table 1. In general, we don't observe obvious mistakes made by our model when visually inspecting results. Fig. 3 shows a random subset of source and predicted targets.

In Table 3 we show the average inference and rendering time of both pixelNeRF and our approach. The inference time is defined as the interval of time required to generate scene information (2D feature maps for pixelNeRF and 3D feature maps for our model) from the source views. The rendering time is the define time required to render a target view given scene information. We compute per-view rendering time and per-object rendering time, where per-object rendering time is accumulated by rendering a total of 250 views. To conduct a fair comparison, we equate the effective image batch size between pixelNeRF and our model. All the run times are reported on an NVIDIA Tesla V100 GPU. As shown in Table 3, our per-view rendering time is $0.0178s$, $100x$ faster than pixelNeRF,

³licensed for non-commercial research purposes

taking 1.9047s to render an image. In other words, our model achieves a rendering speed of 56 FPS, which enables a real-time rendering experience. By amortizing the rendering step across multiple views, our model renders 250 views in 1.022s (245 FPS), while pixelNeRF renders the same 250 views in 474.8606s (0.5 FPS). This translates to over a 400x speedup.

Table 1: Results on category-specific novel view synthesis for ShapeNet chairs and cars. Our method achieves competitive results compared to state-of-the-art approaches.

Data	Methods	1-view		2-view	
		PSNR \uparrow	SSIM \uparrow	PSNR \uparrow	SSIM \uparrow
Chairs	ENR	22.83	-	-	-
	SRN	22.89	0.89	24.48	0.92
	pixelNeRF	23.72	0.91	26.20	0.94
	Ours	23.21	0.92	25.25	0.94
Cars	ENR	22.26	-	-	-
	SRN	22.25	0.89	24.84	0.92
	pixelNeRF	23.17	0.90	25.66	0.94
	Ours	22.83	0.91	24.64	0.93

Table 2: Results on category-specific novel view synthesis for multiple chairs. Compared to pixelNeRF, our method predicts much more coherent synthesis results, and it beats pixelNeRF by a significant margin on all three metrics.

Methods	2-view		
	PSNR \uparrow	SSIM \uparrow	LPIPS \downarrow
SRN	14.67	0.664	0.431
pixelNeRF	23.40	0.832	0.207
Ours	24.13	0.907	0.098

Table 3: Inference and rendering time (in seconds) analysis between pixelNeRF and our method. We show our model can achieve over 100x faster per-frame and over 400x faster per-object rendering speed.

	pixelNeRF		Ours	
	Inference	Rendering	Inference	Rendering
Per-view	0.0053	1.8994	0.0146	0.0032
Per-object	0.0053	474.8553	0.0146	1.0074

4.1.2 Category-Specific View Synthesis of Multiple Objects

We further extend the category-specific evaluation to the multiple-chair dataset proposed by pixelNeRF. This dataset consists of images rendered with two randomly located and oriented chairs. The dataset is designed so that the model cannot simply rely on certain semantic cues such as the symmetric property of a chair to perform geometry completion. The learned model should be flexible and robust enough to represent scenes instead of a single object. All images are rendered with a resolution of 128×128 .

We report reconstruction quality metrics in Table 2. Despite the increased complexity of this setting, our simple model outperforms pixelNeRF across metrics, and exceeds the object-centric method SRN [14] by a large margin. Fig. 4 randomly sampled qualitative results. We observe that the views rendered by our model have cleaner geometry than pixelNeRF, which fails to predict a reasonable geometry at certain angles and suffers from ghosting artifacts.

4.1.3 Category-agnostic View Synthesis

The category-agnostic setting is much more challenging than the category-specific one, because the model needs capacity to jointly learn objects across a range of completely different categories. To evaluate our model in the category-agnostic setting, we follow the same training protocol as baseline method [36] and evaluate on 13 different categories. Each object was rendered in 24 different views with a resolution of 64×64 . We summarize our results in Table 4. Our model beats all baseline methods in every metric. The qualitative visualization in Fig. 5 indicates our model can generate more clean geometry compared to pixelNeRF, which is corroborates the results obtained by our method in the multi-chair dataset.

4.1.4 Unseen-Category View Synthesis

In order to evaluate how our model generalizes to categories not seen during training, we follow the settings in pixelNeRF, and use only three object categories for training, namely airplane, car,

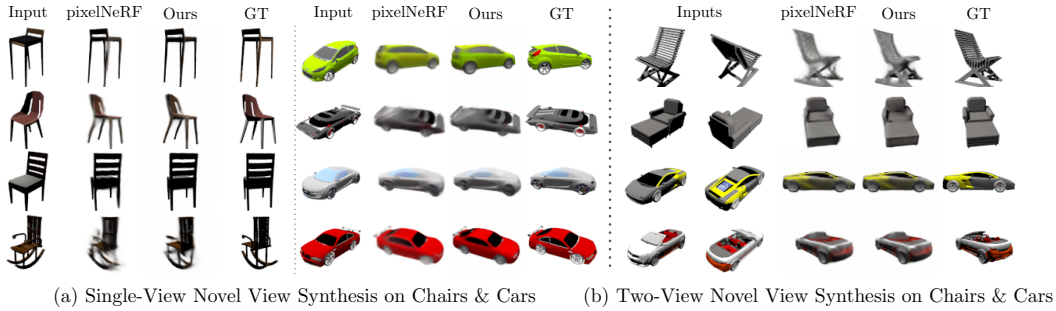


Figure 3: **Qualitative results on category-specific single chair & single car.** The model can either take (a) single view or (b) two views as input to synthesis novel views. We find similar rendering quality comparing to pixelNeRF.

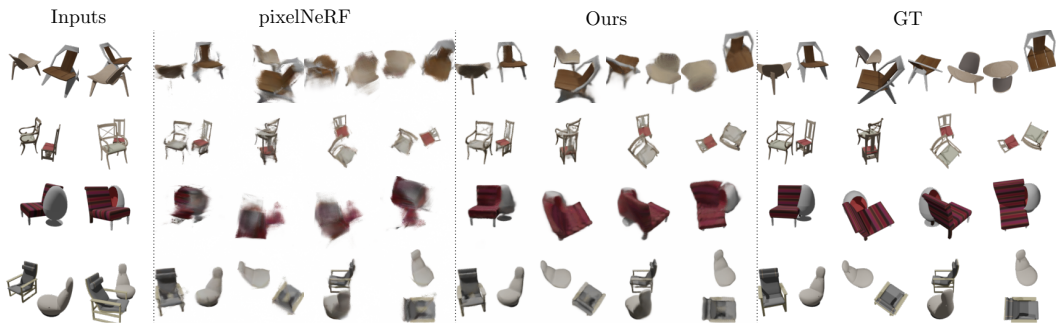


Figure 4: **Qualitative results on category-specific multiple chairs.** The models take two-view images as input. Compared to pixelNeRF, our model renders a cleaner appearance and more complete geometry for chairs with complex shapes.

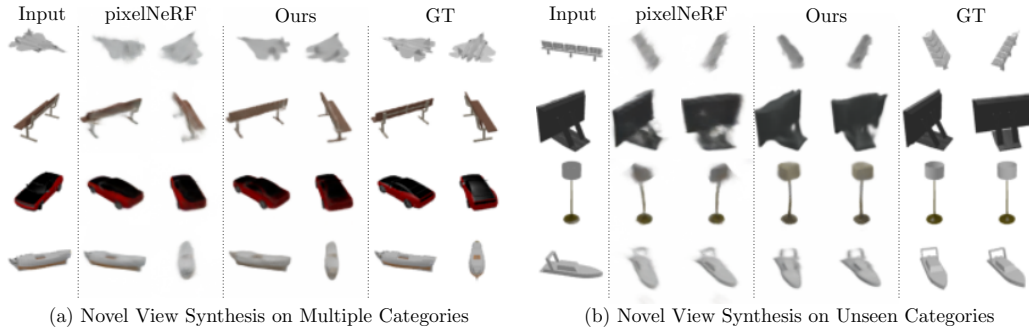


Figure 5: **Qualitative results on (a) category-agnostic and (b) unseen-category datasets.** We test the capacity of our model by training it across different categories in a single-view setting. We evaluate the performance on both seen and unseen categories. We consistently observe cleaner views predicted by our model compared to the baseline.

and chair. We then evaluate on 10 unseen object categories. Table 5 compares the performance of our method with several baselines. We achieve state-of-the-art performance in SSIM and LPIPS, while performing slightly worse than pixelNeRF [1] on PSNR. Fig. 5 indicates that our method is able to learn a good object prior, allowing it to generate feasible geometry for unseen categories such as benches and sofas. We also observe that the novel view images predicted by pixelNeRF are consistently more blurry, which explains its better performance on PSNR. On contrary, our model predicts sharp images that are more favorable by human perception, resulting in better metrics like LPIPS.

Table 4: **Quantitative results on category-agnostic view synthesis.** Our model beats all baselines with a noticeable margin in terms of the mean metrics. The LPIPS score for our mode is significant better compared to state-of-the-art methods in all categories.

Metrics	Methods	plane	bench	cbnt.	car	chair	disp.	lamp	spkr.	rifle	sofa	table	phone	boat	mean
PSNR \uparrow	DVR	25.29	22.64	24.47	23.95	19.91	20.86	23.27	20.78	23.44	23.35	21.53	24.18	25.09	22.70
	SRN	26.62	22.20	23.42	24.40	21.85	19.07	22.17	21.04	24.95	23.65	22.45	20.87	25.86	23.28
	pixelNeRF	29.76	26.35	27.72	27.58	23.84	24.22	28.58	24.44	30.60	26.94	25.59	27.13	29.18	26.80
	Ours	30.15	27.01	28.77	27.74	24.13	24.13	28.19	24.85	30.23	27.32	26.18	27.25	28.91	27.08
SSIM \uparrow	DVR	0.905	0.866	0.877	0.909	0.787	0.814	0.849	0.798	0.916	0.868	0.840	0.892	0.902	0.860
	SRN	0.901	0.837	0.831	0.897	0.814	0.744	0.801	0.779	0.913	0.851	0.828	0.811	0.898	0.849
	pixelNeRF	0.956	0.928	0.924	0.946	0.876	0.871	0.914	0.869	0.970	0.919	0.913	0.925	0.940	0.910
	Ours	0.957	0.930	0.925	0.948	0.877	0.871	0.916	0.869	0.970	0.920	0.914	0.926	0.941	0.920
LPIPS \downarrow	DVR	0.095	0.129	0.125	0.098	0.173	0.150	0.172	0.170	0.094	0.119	0.139	0.110	0.116	0.130
	SRN	0.111	0.150	0.147	0.115	0.152	0.197	0.210	0.178	0.111	0.129	0.135	0.165	0.134	0.139
	pixelNeRF	0.084	0.116	0.105	0.095	0.146	0.129	0.114	0.141	0.066	0.116	0.098	0.097	0.111	0.108
	Ours	0.061	0.080	0.076	0.085	0.103	0.105	0.091	0.116	0.048	0.081	0.071	0.080	0.094	0.082

Table 5: **Quantitative results on unseen-category view synthesis.** Our model obtains slightly worse PSNR, similar SSIM and better LPIPS metrics when compared to pixelNeRF.

Metrics	Methods	bench	cbnt.	disp.	lamp	spkr.	rifle	sofa	table	phone	boat	mean
PSNR \uparrow	DVR	18.37	17.19	14.33	18.48	16.09	20.28	18.62	16.20	16.84	22.43	17.72
	SRN	18.71	17.04	15.06	19.26	17.06	23.12	18.76	17.35	15.66	24.97	18.71
	pixelNeRF	23.79	22.85	18.09	22.76	21.22	23.68	24.62	21.65	21.05	26.55	22.71
	Ours	23.10	22.27	17.01	22.15	20.76	23.22	24.20	20.54	19.59	25.77	21.90
SSIM \uparrow	DVR	0.754	0.686	0.601	0.749	0.657	0.858	0.755	0.644	0.731	0.857	0.716
	SRN	0.702	0.626	0.577	0.685	0.633	0.875	0.702	0.617	0.635	0.875	0.684
	pixelNeRF	0.863	0.814	0.687	0.818	0.778	0.899	0.866	0.798	0.801	0.896	0.825
	Ours	0.865	0.819	0.686	0.822	0.785	0.902	0.872	0.792	0.796	0.898	0.825
LPIPS \downarrow	DVR	0.219	0.257	0.306	0.259	0.266	0.158	0.196	0.280	0.245	0.152	0.240
	SRN	0.282	0.314	0.333	0.321	0.289	0.175	0.248	0.315	0.324	0.163	0.280
	pixelNeRF	0.164	0.186	0.271	0.208	0.203	0.141	0.157	0.188	0.207	0.148	0.182
	Ours	0.135	0.156	0.237	0.175	0.173	0.117	0.123	0.152	0.176	0.128	0.150

4.2 3D Reconstruction

We now turn to the task of evaluating the 3D geometry learned by our approach in a self-supervised manner by minimizing a novel view synthesis objective. In this setting, we evaluate 3D reconstruction by taking the mean intersection-over-union (mIoU) over the predicted α volume (the last channel of \mathbf{V}_s) and the corresponding ground truth occupancy volume. We compare our model to several unsupervised 3D reconstruction methods: PrGAN [37], PlatonicGAN/3D [22], Multi.-View [38], and 3DGAN[39]. PlatonicGAN and PrGAN adopt an adversarial approach to learn 3D reconstruction given a single image with a canonical view. For this evaluation, we utilize the model trained with category-agnostic supervision and report results on the *airplane* class as introduced in [22]. The predicted alpha volume is binarized using a threshold $\tau = 0.05$. The ground truth data is obtained from the ShapeNet voxelized volumes [40] and upsampled from 32^3 to 64^3 via nearest-neighbor interpolation. We then calculate the mIoU score and report in Table 6. Results of other models are directly taken from PlatonicGAN [22].

As shown in Table 6, our model predicts accurate 3D reconstruction, outperforming the best baseline by 10% in mIoU. We attribute this boost in performance to the fact that our model can easily tap large quantities of data in a category-agnostic manner. Whereas in GAN approaches like PlatonicGAN category-agnostic training has traditionally been a very an extremely difficult problem, preventing these approach to tap large quantities of data for view synthesis. Fig. 6, shows qualitative 3D reconstruction results where we observe that our model produces accurate 3D models of objects.

Table 6: **Quantitative results for 3D geometry reconstruction on Airplanes class.** Our model outperforms all baseline models in terms of single-view 3D reconstruction.

	PrGAN	PlatonicGAN	Multi.-View	3DGAN	PlatonicGAN 3D	Ours
mIoU \uparrow	0.11	0.20	0.36	0.46	0.44	0.58

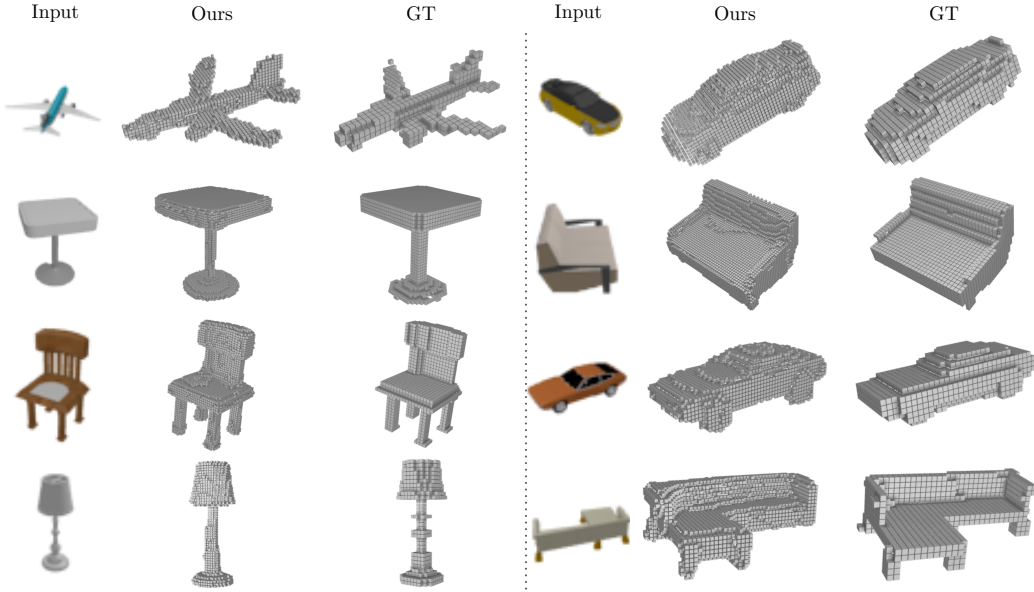


Figure 6: **Qualitative results for 3D geometry reconstruction. (Updated Version)** We visualize the predicted α volume with its raw resolution 64^3 and the ground truth volume with its raw resolution 32^3 . With a single-forward pass, our model can perform 3D geometry reconstruction given a single view of objects from 13 different categories. Our model trained with only 2D supervision consistently predicts meaningful and full geometry.

4.3 Ablation Studies

To better understand the benefits of each component of our model, we perform ablation studies by excluding one of each of the following components: inverse projection, 2D U-Net, 3D U-Net, or halved 3D voxel resolution. We use a 1/4 training split of the ShapeNet chairs dataset and evaluate the performance on the full test split. Table 7 summarizes our findings. Starting from the right-most column, we sequentially remove one of the components and measure the model performance using the PSNR metric. It turns out that each component contributes $[0.1, 0.5]$ metric improvements. The inverse projection component is essential in terms of preserving the implicit geometric and texture information. 2D U-Net and 3D U-Net are useful to synthesize abstract geometry while preserving texture with skip connections. The halved 3D resolution is beneficial in reducing the tensor memory footprint and increasing the receptive field.

Table 7: **Ablation studies on different model components.** We show the effectiveness of various design components in our model, trained with a 1/4 size of the ShapeNet chairs dataset.

	- inverse projection	- 2D U-Net	- 3D U-Net	- half 3D resolution	Full
PSNR	20.62	21.10	21.45	21.82	21.94

5 Conclusion

We have presented a simple yet effective approach to perform novel view synthesis of objects without explicit 3D supervision. Contrary to recent developments using radiance fields for view synthesis, our approach is neither continuous nor implicit. Despite these design choices being claimed as drawbacks that radiance field representations mitigate, we demonstrate that our model obtains comparable or even better performance than recent state-of-the-art approaches using radiance fields, while rendering objects at over 400x speed up. In addition, our model learns accurate 3D geometry in a self-supervised manner, relaxing the need of a large amount of 3D geometry data, and surpassing recent baselines for unsupervised learning of 3D geometry.

References

- [1] A. Yu, V. Ye, M. Tancik, and A. Kanazawa, “pixelnerf: Neural radiance fields from one or few images,” *arXiv preprint arXiv:2012.02190*, 2020.
- [2] A. W. Harley, S. K. Lakshmikanth, P. Schydlo, and K. Fragkiadaki, “Tracking emerges by looking around static scenes, with neural 3d mapping,” in *European Conference on Computer Vision*, pp. 598–614, Springer, 2020.
- [3] M. Prabhudesai, H.-Y. F. Tung, S. A. Javed, M. Sieb, A. W. Harley, and K. Fragkiadaki, “Embodied language grounding with 3d visual feature representations,” in *Proceedings of the IEEE/CVF Conference on Computer Vision and Pattern Recognition*, pp. 2220–2229, 2020.
- [4] H.-Y. F. Tung, R. Cheng, and K. Fragkiadaki, “Learning spatial common sense with geometry-aware recurrent networks,” in *Proceedings of the IEEE/CVF Conference on Computer Vision and Pattern Recognition*, pp. 2595–2603, 2019.
- [5] P. Dai, Y. Zhang, Z. Li, S. Liu, and B. Zeng, “Neural point cloud rendering via multi-plane projection,” in *Proceedings of the IEEE/CVF Conference on Computer Vision and Pattern Recognition*, pp. 7830–7839, 2020.
- [6] P. P. Srinivasan, R. Tucker, J. T. Barron, R. Ramamoorthi, R. Ng, and N. Snavely, “Pushing the boundaries of view extrapolation with multiplane images,” in *Proceedings of the IEEE/CVF Conference on Computer Vision and Pattern Recognition*, pp. 175–184, 2019.
- [7] T. Zhou, R. Tucker, J. Flynn, G. Fyffe, and N. Snavely, “Stereo magnification: Learning view synthesis using multiplane images,” *arXiv preprint arXiv:1805.09817*, 2018.
- [8] B. Mildenhall, P. P. Srinivasan, R. Ortiz-Cayon, N. K. Kalantari, R. Ramamoorthi, R. Ng, and A. Kar, “Local light field fusion: Practical view synthesis with prescriptive sampling guidelines,” *ACM Transactions on Graphics (TOG)*, vol. 38, no. 4, pp. 1–14, 2019.
- [9] T. Zhou, S. Tulsiani, W. Sun, J. Malik, and A. A. Efros, “View synthesis by appearance flow,” in *European conference on computer vision*, pp. 286–301, Springer, 2016.
- [10] S.-H. Sun, M. Huh, Y.-H. Liao, N. Zhang, and J. J. Lim, “Multi-view to novel view: Synthesizing novel views with self-learned confidence,” in *Proceedings of the European Conference on Computer Vision (ECCV)*, pp. 155–171, 2018.
- [11] K.-A. Aliev, D. Ulyanov, and V. Lempitsky, “Neural point-based graphics,” *arXiv preprint arXiv:1906.08240*, vol. 2, no. 3, p. 4, 2019.
- [12] S. Liu, T. Li, W. Chen, and H. Li, “Soft rasterizer: A differentiable renderer for image-based 3d reasoning,” in *Proceedings of the IEEE/CVF International Conference on Computer Vision*, pp. 7708–7717, 2019.
- [13] E. Dupont, M. A. Bautista, A. Colburn, A. Sankar, C. Guestrin, J. Susskind, and Q. Shan, “Equivariant neural rendering,” *arXiv preprint arXiv:2006.07630*, 2020.
- [14] V. Sitzmann, M. Zollhöfer, and G. Wetzstein, “Scene representation networks: Continuous 3d-structure-aware neural scene representations,” in *Advances in Neural Information Processing Systems*, pp. 1121–1132, 2019.
- [15] B. Mildenhall, P. P. Srinivasan, M. Tancik, J. T. Barron, R. Ramamoorthi, and R. Ng, “Nerf: Representing scenes as neural radiance fields for view synthesis,” *arXiv preprint arXiv:2003.08934*, 2020.
- [16] A. Trevithick and B. Yang, “Grf: Learning a general radiance field for 3d scene representation and rendering,” *arXiv preprint arXiv:2010.04595*, 2020.
- [17] K. Park, U. Sinha, J. T. Barron, S. Bouaziz, D. B. Goldman, S. M. Seitz, and R.-M. Brullalla, “Deformable neural radiance fields,” *arXiv preprint arXiv:2011.12948*, 2020.
- [18] D. Rebain, W. Jiang, S. Yazdani, K. Li, K. M. Yi, and A. Tagliasacchi, “Derf: Decomposed radiance fields,” *arXiv preprint arXiv:2011.12490*, 2020.
- [19] I. Choi, O. Gallo, A. Troccoli, M. H. Kim, and J. Kautz, “Extreme view synthesis,” in *Proceedings of the IEEE/CVF International Conference on Computer Vision*, pp. 7781–7790, 2019.

- [20] X. Chen, J. Song, and O. Hilliges, “Monocular neural image based rendering with continuous view control,” in *Proceedings of the IEEE/CVF International Conference on Computer Vision*, pp. 4090–4100, 2019.
- [21] K. Olszewski, S. Tulyakov, O. Woodford, H. Li, and L. Luo, “Transformable bottleneck networks,” in *Proceedings of the IEEE International Conference on Computer Vision*, pp. 7648–7657, 2019.
- [22] P. Henzler, N. J. Mitra, and T. Ritschel, “Escaping plato’s cave: 3d shape from adversarial rendering,” in *Proceedings of the IEEE International Conference on Computer Vision*, pp. 9984–9993, 2019.
- [23] K. Rematas, R. Martin-Brualla, and V. Ferrari, “Sharf: Shape-conditioned radiance fields from a single view,” *arXiv preprint arXiv:2102.08860*, 2021.
- [24] Q. Wang, Z. Wang, K. Genova, P. Srinivasan, H. Zhou, J. T. Barron, R. Martin-Brualla, N. Snavely, and T. Funkhouser, “Ibrnet: Learning multi-view image-based rendering,” *arXiv preprint arXiv:2102.13090*, 2021.
- [25] A. Yu, R. Li, M. Tancik, H. Li, R. Ng, and A. Kanazawa, “Plenotrees for real-time rendering of neural radiance fields,” *arXiv preprint arXiv:2103.14024*, 2021.
- [26] S. J. Garbin, M. Kowalski, M. Johnson, J. Shotton, and J. Valentin, “Fastnerf: High-fidelity neural rendering at 200fps,” *arXiv preprint arXiv:2103.10380*, 2021.
- [27] S. Wizarawongsa, P. Phongthawee, J. Yenphraphai, and S. Suwajanakorn, “Nex: Real-time view synthesis with neural basis expansion,” *arXiv preprint arXiv:2103.05606*, 2021.
- [28] O. Ronneberger, P. Fischer, and T. Brox, “U-net: Convolutional networks for biomedical image segmentation,” in *International Conference on Medical image computing and computer-assisted intervention*, pp. 234–241, Springer, 2015.
- [29] Z. Murez, T. van As, J. Bartolozzi, A. Sinha, V. Badrinarayanan, and A. Rabinovich, “Atlas: End-to-end 3d scene reconstruction from posed images,” *arXiv preprint arXiv:2003.10432*, 2020.
- [30] J. T. Kajiya and B. P. Von Herzen, “Ray tracing volume densities,” *ACM SIGGRAPH computer graphics*, vol. 18, no. 3, pp. 165–174, 1984.
- [31] M. Jaderberg, K. Simonyan, A. Zisserman, and K. Kavukcuoglu, “Spatial transformer networks,” *arXiv preprint arXiv:1506.02025*, 2015.
- [32] Z. Wang, A. Bovik, H. Sheikh, and E. Simoncelli, “Image quality assessment: from error visibility to structural similarity,” *IEEE Transactions on Image Processing*, vol. 13, no. 4, pp. 600–612, 2004.
- [33] A. X. Chang, T. Funkhouser, L. Guibas, P. Hanrahan, Q. Huang, Z. Li, S. Savarese, M. Savva, S. Song, H. Su, *et al.*, “Shapenet: An information-rich 3d model repository,” *arXiv preprint arXiv:1512.03012*, 2015.
- [34] M. Niemeyer, L. Mescheder, M. Oechsle, and A. Geiger, “Differentiable volumetric rendering: Learning implicit 3d representations without 3d supervision,” in *Proceedings of the IEEE/CVF Conference on Computer Vision and Pattern Recognition*, pp. 3504–3515, 2020.
- [35] R. Zhang, P. Isola, A. A. Efros, E. Shechtman, and O. Wang, “The unreasonable effectiveness of deep features as a perceptual metric,” in *Proceedings of the IEEE conference on computer vision and pattern recognition*, pp. 586–595, 2018.
- [36] H. Kato, Y. Ushiku, and T. Harada, “Neural 3d mesh renderer,” 2017.
- [37] T. Karras, T. Aila, S. Laine, and J. Lehtinen, “Progressive growing of gans for improved quality, stability, and variation,” *arXiv preprint arXiv:1710.10196*, 2017.
- [38] X. Yan, J. Yang, E. Yumer, Y. Guo, and H. Lee, “Perspective transformer nets: Learning single-view 3d object reconstruction without 3d supervision,” *arXiv preprint arXiv:1612.00814*, 2016.
- [39] J. Wu, C. Zhang, T. Xue, W. T. Freeman, and J. B. Tenenbaum, “Learning a probabilistic latent space of object shapes via 3d generative-adversarial modeling,” *arXiv preprint arXiv:1610.07584*, 2016.

- [40] C. B. Choy, D. Xu, J. Gwak, K. Chen, and S. Savarese, “3d-r2n2: A unified approach for single and multi-view 3d object reconstruction,” in *Proceedings of the European Conference on Computer Vision (ECCV)*, 2016.
- [41] K. He, X. Zhang, S. Ren, and J. Sun, “Deep residual learning for image recognition,” 2015.
- [42] Y. Wu and K. He, “Group normalization,” 2018.
- [43] A. Kar, C. Häne, and J. Malik, “Learning a multi-view stereo machine,” 2017.
- [44] J. Krause, M. Stark, J. Deng, and L. Fei-Fei, “3d object representations for fine-grained categorization,” in *4th International IEEE Workshop on 3D Representation and Recognition (3dRR-13)*, (Sydney, Australia), 2013.
- [45] A. Kirillov, Y. Wu, K. He, and R. Girshick, “Pointrend: Image segmentation as rendering,” 2020.

A Limitations of the Work

Though our model shows very promising reconstruction results and great efficiency, a few limitations still exist to be tackled as future work. First, training a high fidelity as well as scene/category-agnostic representation remains an open problem for both explicit and implicit methods. The resolution of images that can be rendered by our model is capped by the resolution of the explicit voxel-like scene representation. Different from our approach, continuous representations like radiance fields are resolution-free by definition; however, they are either slow to obtain or slow to render. As a future work, we plan to investigate the use of different explicit representations like octree to increase our model capacity for non-empty and complex regions of space. Second, our current model cannot produce view-dependent effects. We leave this as future work to be tackled with a more advanced rendering equation and more informative scene representation that incorporates view direction, surface information, etc.

B Social Impact

Our work represents a step towards producing highly realistic generative models of the world. Such a goal can have both positive and negative social impacts. On the positive side, our model can enable interactive art creation, improved AR/VR experiences, etc. On the negative side, better generative models of 3D objects can potentially be misused to produce technology similar to deep fakes that have become a concern for misrepresenting person identity. Releasing code, models, and technical papers can help the community prepare for this kind of misuse by detecting fake content or ensuring content is certified.

C Experiment Details

C.1 Implementation Details

The 2D feature encoder utilizes the U-Net [28] with a ResNet-18 [41] backbone, initialized with ImageNet pre-trained weights. The intermediate feature channels are 64, 128, 256, 512 at each spatial resolution level during downsampling. At the upsampling stage, we perform deconvolution and fuse the resulting features with skip encoder features at the same level through concatenation followed by two consecutive convolution blocks. The final 2D feature map has the same spatial resolution as the input image, with a 32 channel feature map.

At the inverse projection stage, the 2D feature map is back-projected into a 3D voxel space that has halved spatial height and width with respect to the input feature map. To enable back-projection, we first tile the 2D features into a 3D cube to prepare for sampling the inverse projection. Next, we leverage the camera intrinsic parameters to compute the homography matrix to map the cube to the viewing frustum. The grid mapping function is obtained by multiplying the homography matrix with individual points from the fixed voxel mesh grid set. Lastly, we apply the *grid_sample* function to perform the inverse projection.

The 3D feature decoder consists of a 3D U-Net with ResNet-3D blocks. Following common practice, when spatial resolution is downsampled by 2 times, we double the channel numbers. The output 3D

feature map has 16 channels with the same spatial resolution as the input image. At the final layer, we apply one 3D convolution to transform the tensor map into 4 channels and sigmoid activations to produce the RGB_α volume.

At the amortized rendering stage, we combine the rotation transformation and the perspective deformation into one by left matrix multiplication, where rotation transformation transfers a volume from the source view to the target view and perspective deformation maps the viewing frustum to the output cube. After similar mesh grid multiplication and grid sampling steps as in inverse projection, we obtain the voxel volume used for alpha blending. The alpha blending process leverages *cumprod* method to calculate the accumulated transmittance between the near plane and the current point.

We use the ReLU nonlinearity and GroupNorm [42] normalization throughout the model for each nonlinear transformation. We train the network for 150 epochs with Adam optimizer and a fixed learning rate of 0.0016, the loss weighting for SSIM [32] loss is set to be 0.05. We only perform data normalization with ImageNet statistics at the preprocessing stage.

C.2 Computation Resources

For the category-specific view synthesis, each model is trained using 30 V100 GPUs on an internal cluster. It takes 5 days to train the single-chair dataset, 2.5 days to train the single-car dataset, and 1.5 days to train the multiple-chair dataset.

For the category-agnostic and unseen-category view synthesis, each model is trained using 30 V100 GPUs on an internal cluster, and it takes us 2.5 days to train each dataset.

We are able to perform the evaluation on a single GPU in minutes compared to PixelNeRF[1], which takes days for evaluation.

D Additional Experiments & Visualizations

D.1 Additional Experiments for Unseen-Category View Synthesis

To further demonstrate the generalization capacity of our method, we extend the baselines for unseen-category view synthesis experiments to include ENR[13]. Our proposed approach beats ENR [13] in all metrics as shown in Table 8. Figure 7 also shows that our model is able to synthesize objects with more clean geometry (less blurry artifacts) as seen from the visualizations of boat (row 1), bench (row 7) objects. In addition, we also report results for a two-view model. During training, we randomly sample pairs of source images as input; during evaluation, we sample two images offset by 90 degrees azimuth as input. Figure 7 shows this model is not biased towards the training categories anymore, instead, the model is learning to perform view synthesis given two views of an unseen object.

Table 8: **Quantitative results on unseen-category view synthesis.** Our model bypasses ENR [13] baseline by a noticeable margin. Our two-view model has a very large improvement from single-view counterpart, which indicates the good generalizability of the model.

Metrics	Methods	bench	cbnt.	disp.	lamp	spkr.	rifle	sofa	table	phone	boat	mean
PSNR \uparrow	ENR	22.59	21.41	16.99	22.29	20.13	23.22	23.16	20.00	20.15	25.81	21.50
	Ours (Single-View)	23.10	22.27	17.01	22.15	20.76	23.22	24.20	20.54	19.59	25.77	21.90
	Ours (Two-View)	25.11	24.54	20.85	25.19	22.72	27.74	26.24	23.34	23.80	29.17	24.80
SSIM \uparrow	ENR	0.845	0.799	0.674	0.819	0.768	0.900	0.848	0.759	0.806	0.896	0.807
	Ours (Single-View)	0.865	0.819	0.686	0.822	0.785	0.902	0.872	0.792	0.796	0.898	0.825
	Ours (Two-View)	0.909	0.875	0.818	0.905	0.838	0.963	0.913	0.871	0.897	0.950	0.893
LPIPS \downarrow	ENR	0.182	0.199	0.273	0.203	0.202	0.143	0.166	0.206	0.182	0.154	0.190
	Ours (Single-View)	0.135	0.156	0.237	0.175	0.173	0.117	0.123	0.152	0.176	0.128	0.150
	Ours (Two-View)	0.108	0.122	0.153	0.118	0.140	0.072	0.098	0.106	0.107	0.087	0.107

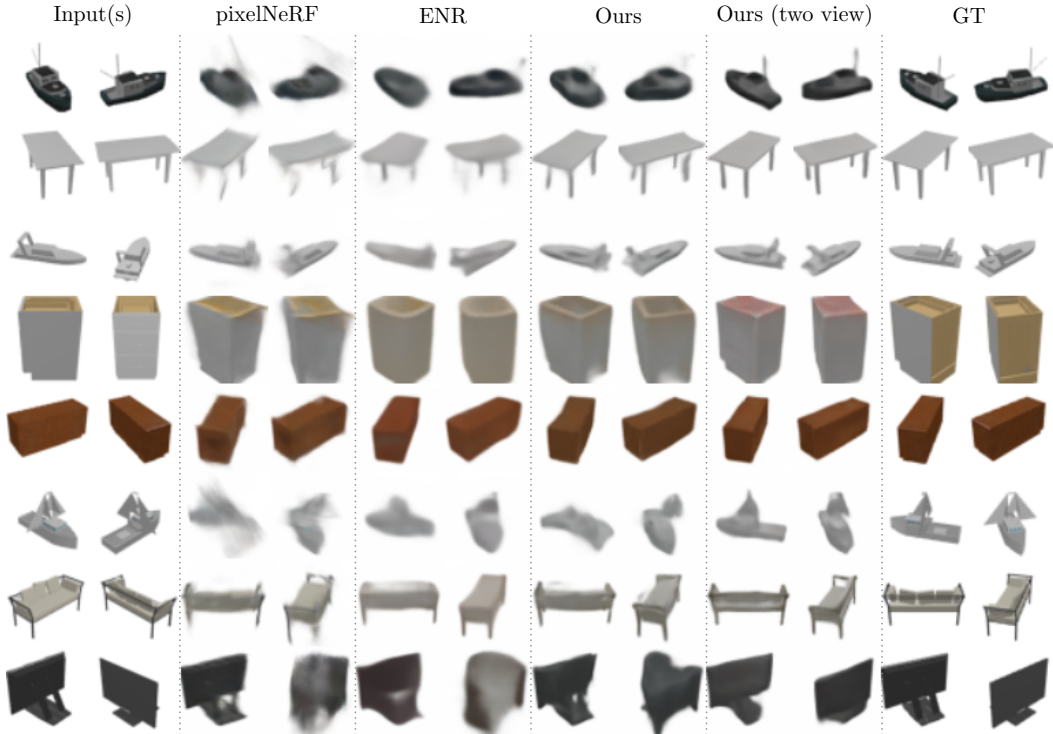


Figure 7: **Qualitative results on unseen-category datasets.** All methods except ours (two view) tasks a single input view (left image under Input(s) column) and perform novel view synthesis.

D.2 Additional Experiments for 3D Reconstruction

We further demonstrate the 3D reconstruction performance of our model by comparing with two **supervised** 3D reconstruction baselines V-LSMs[43] and 3D-R2N2 [40]. These baselines use voxel occupancy as supervision, while our model only relies on 2D self-supervision. To conduct a fair comparison, we downsampled the predicted voxel from 64^3 to 32^3 and utilize the same thresholding strategy as reported in Section 4.2. Table 9 indicates that our model obtains better mIoU on 9 out of 13 categories of objects and better mean mIoU across categories.

Table 9: **Quantitative results for 3D geometry reconstruction on 13 ShapeNet classes.** Our model has better mIoU metric compared to V-LSMs[43] and 3D-R2N2 [40] (1-view) that leverage groundtruth voxel occupancies as the supervision signal.

Metrics	Methods	plane	bench	cbnt.	car	chair	disp.	lamp	spkr.	rifle	sofa	table	phone	boat	mean
mIoU \uparrow	3D-R2N2 w/pose [40] (1 view)	56.7	43.2	61.8	77.6	50.9	44.0	40.0	56.7	56.5	58.9	51.6	65.6	53.1	55.1
	V-LSMs[43] (1 view)	61.1	50.8	65.9	79.3	57.8	53.9	48.1	63.9	69.7	67.0	55.6	67.7	58.3	61.5
	Ours (1 view)	57.7	54.7	76.0	80.4	57.0	60.6	51.8	74.1	60.2	72.3	53.8	72.0	60.0	63.25

D.3 Real Car View Synthesis

We also test our model generalization capabilities when transferring to a new target domain. We use the model trained with ShapeNet synthetic car objects from Section 4.1.1 of the main text and perform novel view synthesis on real car images from [44]. Following the same protocol as pixelNeRF [1], we masked out the background and paint as white using PointRend[45], and perform view synthesis in input view coordinate space. Figure 8 suggests that our model can predict plausible novel views of the real cars. The geometry is similar to pixelNeRF[1] results with less artifacts and blurry effects.



Figure 8: **Qualitative results for Real Car Image.** We use the model trained with ShapeNet virtual cars objects and perform novel view synthesis on real car images. Our model is able to synthesize plausible novel views, similar to pixelNeRF[1] but with less blurry effects.

D.4 Increasing Number of Source Views on Category-specific Multiple Chairs

We analyze the capability of our model in terms of handling different numbers of source views. In this experiment, we use a model trained with two source views for evaluation. As shown in Table 10 and Figure 9, our model’s performance decreases on the one view setting due to having to deal with a large number of degrees of freedom. As the number of source view increases, the model is able to satisfy more constraints; our model achieves the best performance in the three-view setting.

Table 10: **Quantitative results on category-specific multiple chairs with increased number of views.**

Methods	1-view			2-view			3-view		
	PSNR \uparrow	SSIM \uparrow	LPIPS \downarrow	PSNR \uparrow	SSIM \uparrow	LPIPS \downarrow	PSNR \uparrow	SSIM \uparrow	LPIPS \downarrow
Ours	17.02	0.747	0.241	24.13	0.907	0.098	26.18	0.935	0.076

D.5 Additional Visualizations

We include additional visualizations for every experiment:

- Figure 10: category-specific single chair dataset with one source view;
- Figure 11: category-specific single chair dataset with two source views;
- Figure 12: category-specific single car dataset with one source view;
- Figure 13: category-specific single car dataset with two source views;
- Figure 14: category-specific multiple chairs dataset;
- Figure 15: category-agnostic dataset;
- Figure 16: unseen-category dataset.

We intentionally use the same random indices for different view settings of the single chair/car dataset. From the visualizations in Figure 10 v.s. Figure 11 and Figure 12 v.s. Figure 13, it can be easily observed that our model can synthesize better geometry and texture at novel target pose with more information given. Under the folder `supp/gifs` in this supplementary, you can find gifs for visualizations of all experiments. In each gif, the novel views predicted by our model are shown on the left, ground truth views are shown on the right. The gifs are named with pattern: `object id_source view index.gif`.

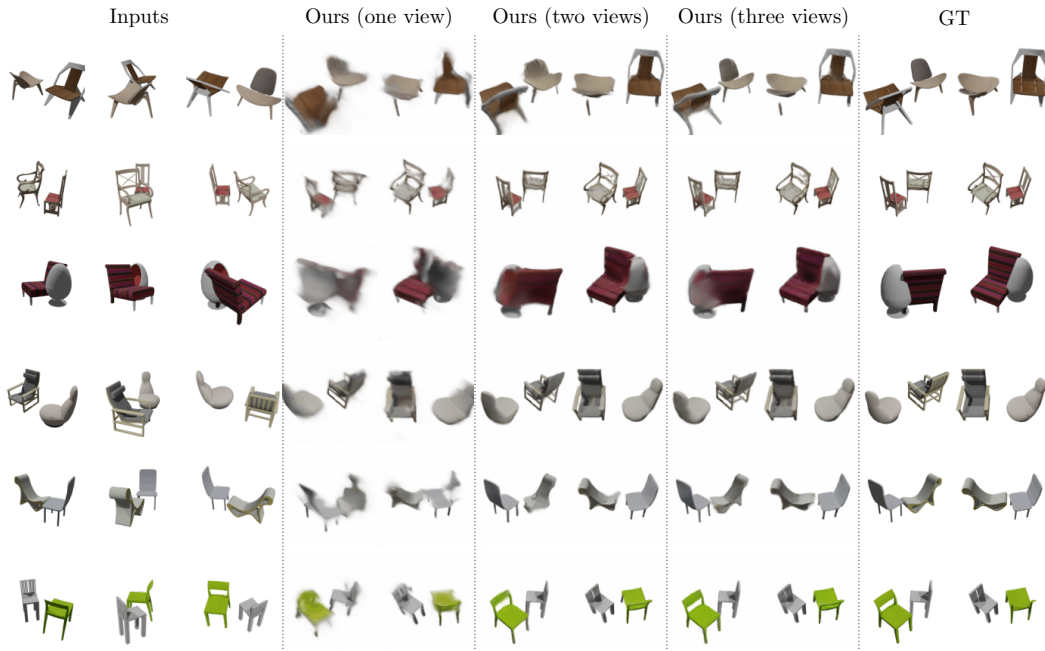


Figure 9: **Qualitative results on category-specific multiple chairs with an increased number of views.** We apply our model only trained with two input source viewers to a different number of input views settings during evaluation. Our model can predict better geometries and textures with the increasing number of views.

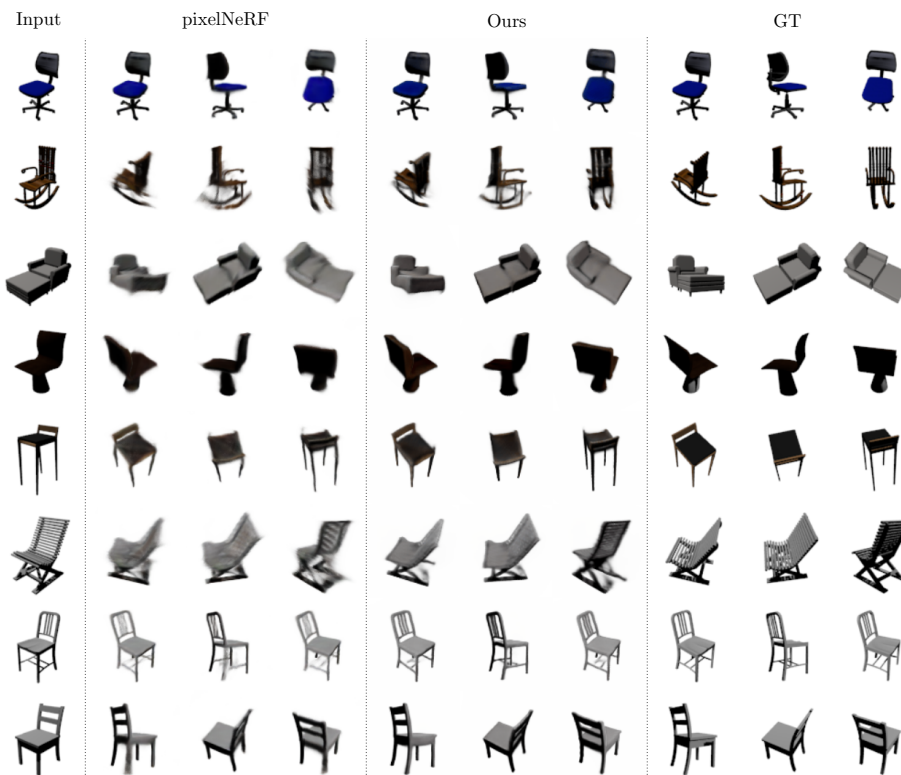


Figure 10: **Qualitative results on category-specific single chair (single-view)**

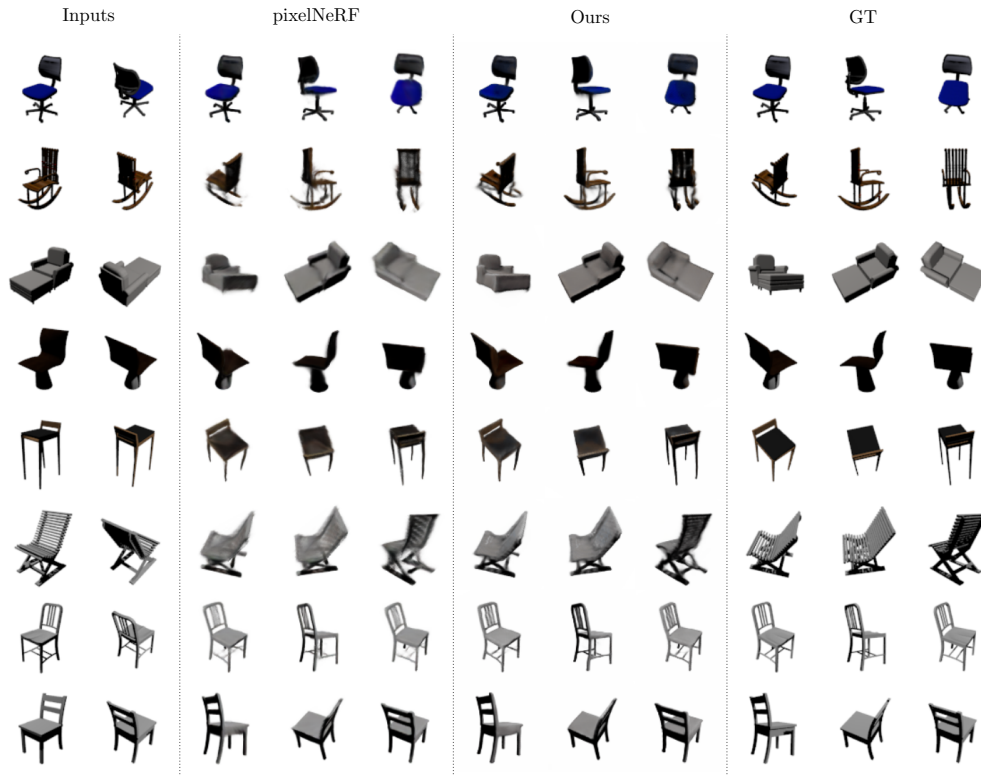


Figure 11: Qualitative results on category-specific single chair (two-view)

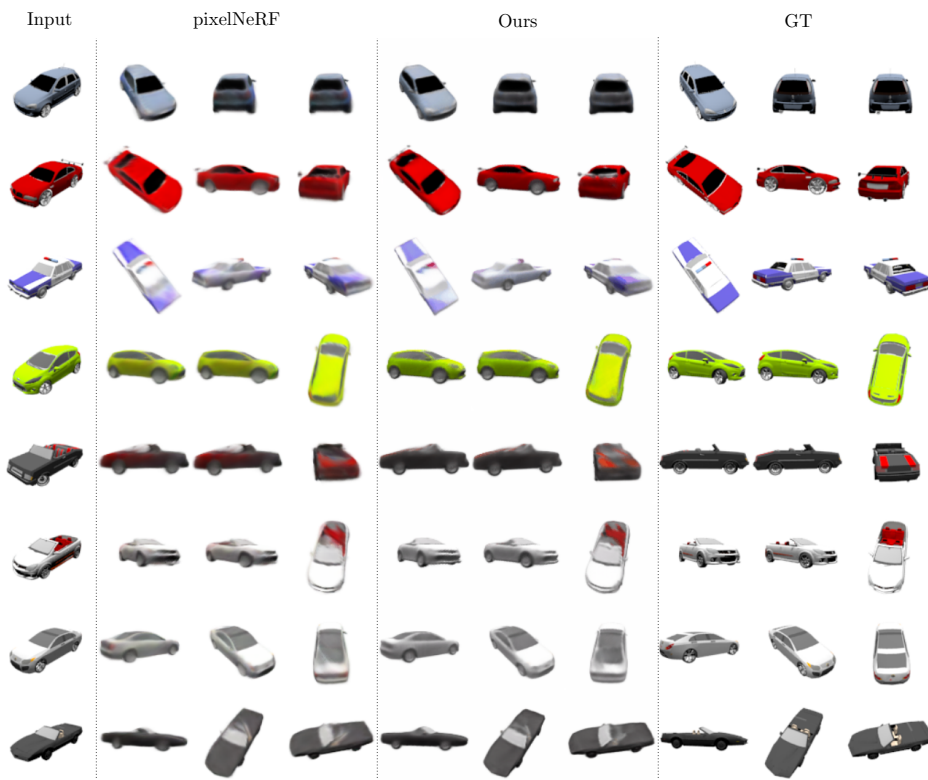


Figure 12: Qualitative results on category-specific single car (single-view)

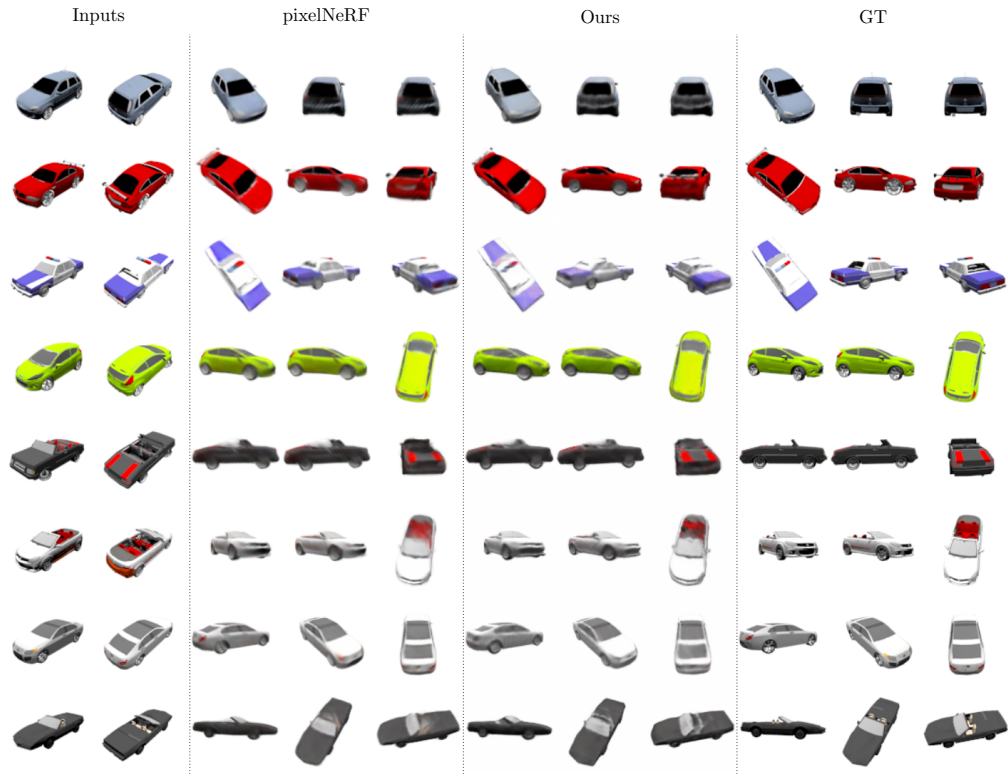


Figure 13: Qualitative results on category-specific single car (two-view)

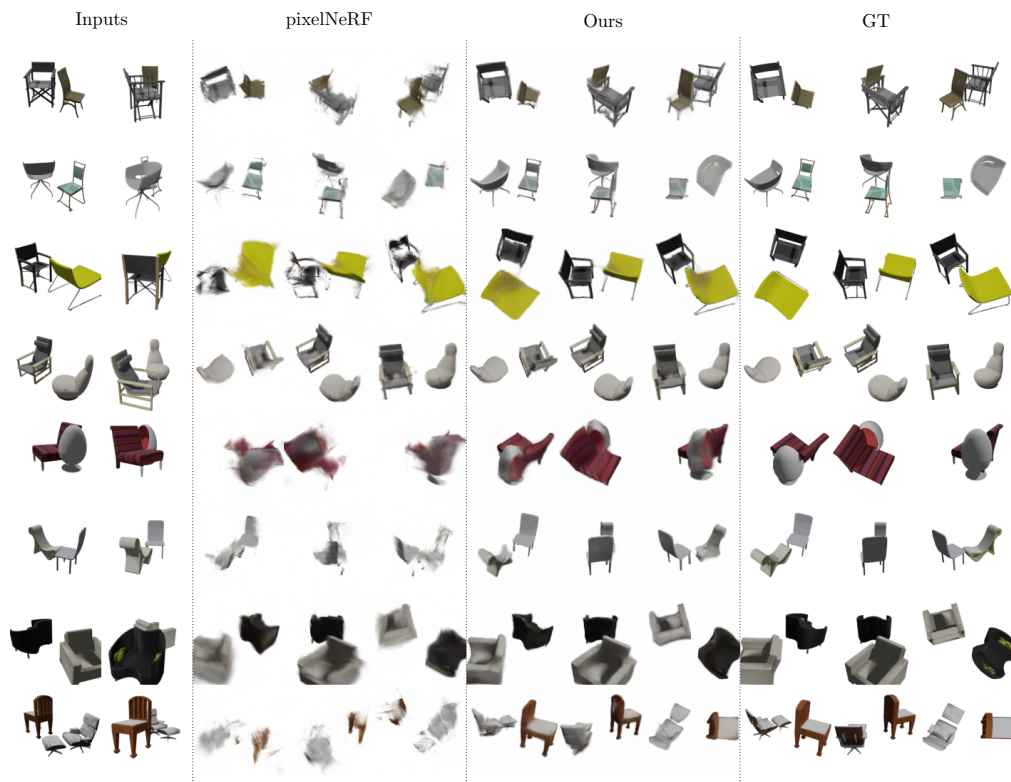


Figure 14: Qualitative results on category-specific multiple chairs (two-view)

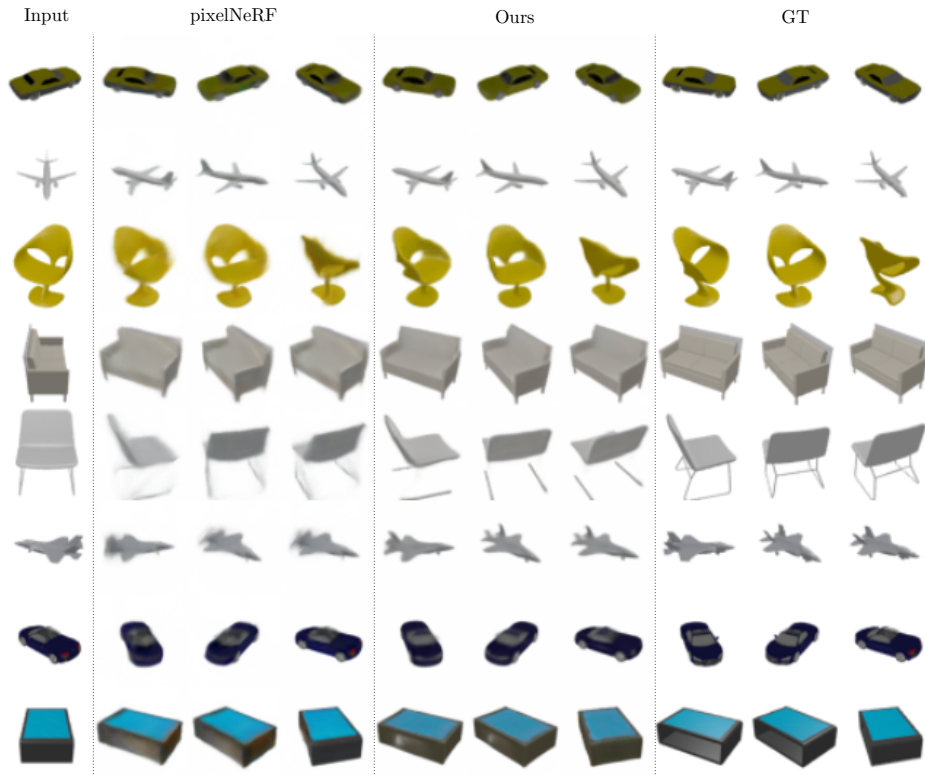


Figure 15: Qualitative results on multiple-category dataset (one-view)

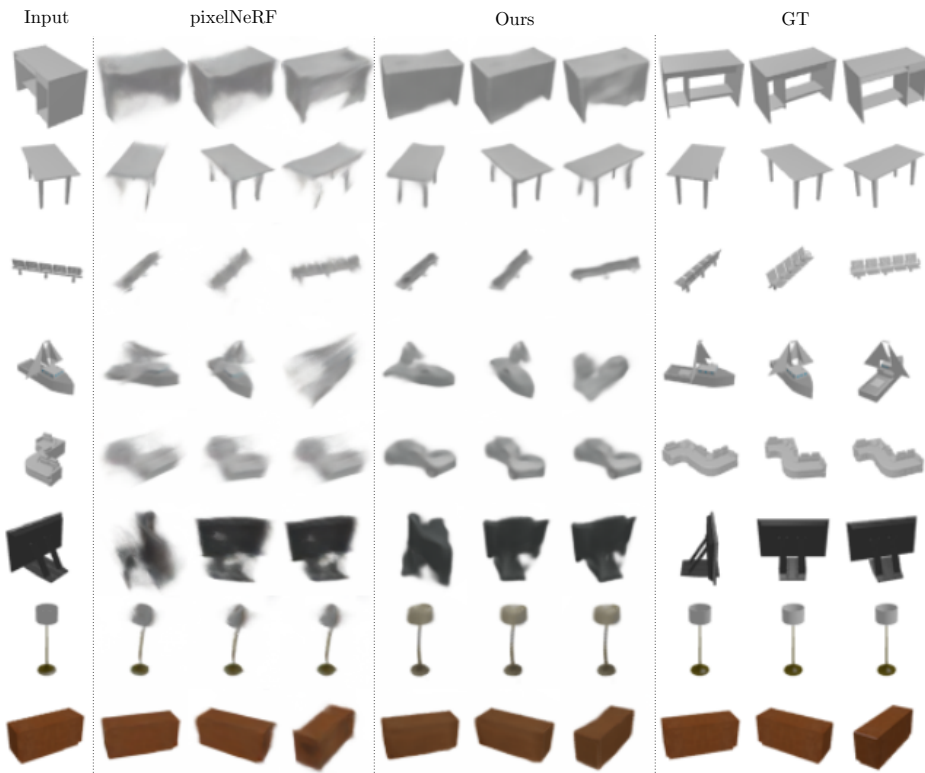


Figure 16: Qualitative results on unseen-category dataset (one-view)